Limitations of rupture forecasting exposed by instantaneously triggered earthquake doublet

E. Nissen[1]*, J. R. Elliott[2], R. A. Sloan[2,3], T. J. Craig[4], G. J. Funning[5], A. Hutko[6], B. E. Parsons[2] and T. J. Wright[4]

Earthquake hazard assessments and rupture forecasts are based on the potential length of seismic rupture and whether or not slip is arrested at fault segment boundaries. Such forecasts do not generally consider that one earthquake can trigger a second large event, near-instantaneously, at distances greater than a few kilometres. Here we present a geodetic and seismological analysis of a magnitude 7.1 intracontinental earthquake that occurred in Pakistan in 1997. We find that the earthquake, rather than a single event as hitherto assumed, was in fact an earthquake doublet: initial rupture on a shallow, blind reverse fault was followed just 19 s later by a second rupture on a separate reverse fault 50 km away. Slip on the second fault increased the total seismic moment by half, and doubled both the combined event duration and the area of maximum ground shaking. We infer that static Coulomb stresses at the initiation location of the second earthquake were probably reduced as a result of the first. Instead, we suggest that a dynamic triggering mechanism is likely, although the responsible seismic wave phase is unclear. Our results expose a flaw in earthquake rupture forecasts that disregard cascading, multiple-fault ruptures of this type.

Continental earthquakes typically rupture diffuse systems of shallow fault segments, delineated by bends, step-overs, gaps and terminations. The largest events generally involve slip on multiple segments and whether or not rupture is arrested by these boundaries can determine the difference between a moderate earthquake and a potentially devastating one. Compilations of historical surface ruptures suggest that boundary offsets of ∼5 km are sufficient to halt earthquakes, regardless of the total rupture length[1,2]. This value is incorporated into modern, fault-based earthquake rupture forecasts such as the UCERF3 model for California[3,4], whose goals include anticipating the maximum possible rupture length and magnitude of future earthquakes within known fault systems.

However, if earthquakes could rapidly trigger failure of neighbouring faults or fault segments, at distances larger than ∼5 km, then such scenario planning could be missing an important class of cascading, multiple-fault rupture. Here we exploit the combination of spatial information captured by satellite deformation measurements and timing information of successive fault ruptures from seismology, to reveal how near-instantaneous, probably dynamic triggering may lead to sequential rupture of multiple large earthquakes separated by distances of tens of kilometres.

The destructive Harnai earthquake occurred on 27 February 1997 at 21:08 UTC (2:08 on 28 February, local time) in the western Sulaiman mountains of Pakistan[5] (Fig. 1a). Published source catalogues ascribe it a single, largely (85–99%) double-couple focal mechanism with gentle approximately north-dipping and steep approximately south-dipping nodal planes and a moment magnitude M_w of 7.0–7.1 (Supplementary Table 1). The largest catalogued aftershocks include a surface wave magnitude M_s 6.4 event that struck 22 min after the mainshock at 21:30 UTC, and seven further earthquakes of $M > 5.0$ during the next ten months.

There were no reports of surface rupturing in any of these events. The Sulaiman mountains lie within the western boundary zone of the India–Eurasia collision where Palaeozoic–Palaeogene Indian passive margin sediments and Neogene flysch and molasse are folded and thrust over rigid Indian basement[6–9] (inset, Fig. 1a and Supplementary Fig. 1). Cover thicknesses increase from 8–10 km within the low-lying Sibi Trough, south of the range, to 15–20 km in the range interior[10–12]. Past instrumental seismicity is dominated by reverse-faulting earthquakes with centroid depths of <10 km, steeply dipping (30°–60°) nodal planes roughly aligned with local surface folding, and P axes oriented radially to the curved mountain front as if gravitational forces arising from the topography are important in driving deformation[8,10,13–16].

Surface deformation from InSAR

We mapped the surface deformation in the Harnai earthquake with Interferometric Synthetic Aperture Radar (InSAR), using two images captured on 6 May 1996 and 31 May 1999 by the European Space Agency European Remote Sensing (ERS-2) satellite (see Methods). The descending-track satellite line of sight has an azimuth of 283° and is inclined at 23° from the vertical at the scene centre. The interferogram (Fig. 1b) contains a near-continuous signal in mountainous areas but is decorrelated over most of the Sibi Trough, probably owing to agriculture. It contains two distinct fringe ellipses containing displacements towards the satellite, characteristic of slip on buried thrust or reverse faults: one in the scene centre and one in the southeastern corner of the interferogram. The unwrapped interferogram contains peak displacements of ∼60 cm towards the satellite in the central deformation patch and ∼50 cm towards the satellite in the southeastern one (Fig. 1c). The southeastern fringe pattern is partially obscured by an incoherent region
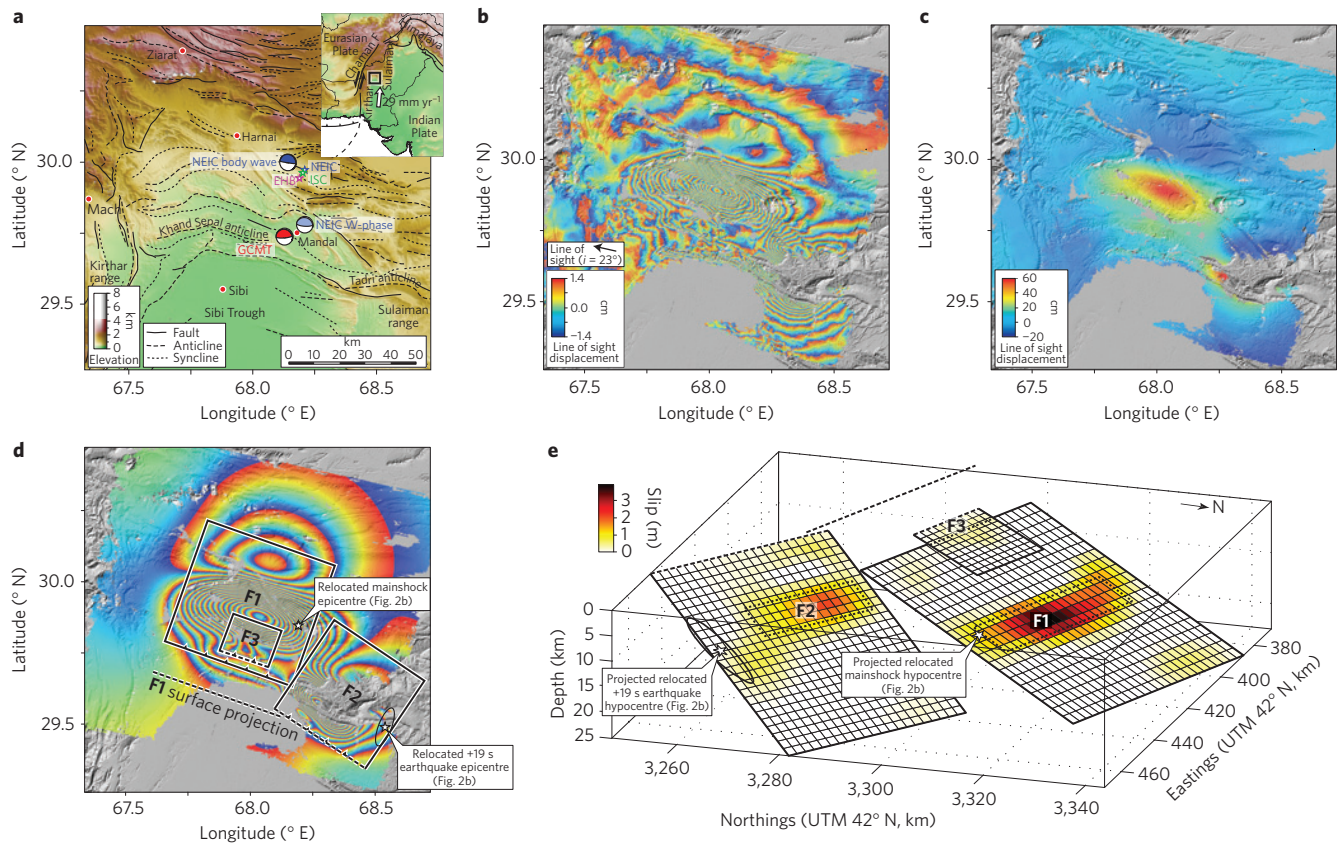
Figure 1 | Tectonic setting and InSAR data and modelling results. a, Tectonic setting with published epicentres and focal mechanisms for the 27 February 1997 earthquake from the USGS National Earthquake Information Center (NEIC, in blue), the International Seismological Centre (ISC, green), the Engdahl, van der Hilst and Bulland catalogue[49] (EHB, magenta), and the Global Centroid Moment Tensor project (GCMT, red). Inset shows tectonic setting with the local motion of India relative to Eurasia[50]. **b,c**, Wrapped (**b**) and unwrapped (**c**) interferogram spanning the mainshock and major aftershocks (6 May 1996–31 May 1999). **d**, Model interferogram and faults, with up-dip surface projections marked by dashed lines. **e**, Model slip view with extents of initial uniform slip model faults indicated by dotted rectangles.

where high deformation gradients or mass movements may have caused decorrelation.

To characterize the causative faulting we used elastic dislocation modelling[17,18] guided where possible by independent constraints from seismology (see Methods). The broad fringe ellipse in the scene centre corresponds to slip on a buried, north-northeast-dipping, shallow-angle (21°) reverse fault (labelled F1 in Fig. 1d,e) with a moment magnitude of 7.0. Slip is centred at a depth of ~15 km, consistent with the estimated depth of the basement–sedimentary cover interface in this area[12]. Seismic slip along this interface would rule out the existence of a weak decollement of the kind that underlies the lobate Sulaiman range to the east. Whereas the apex of the Sulaiman range can propagate southwards, facilitated by foreland sediments that are weaker and/or thicker than in neighbouring parts of the Indian Plate[8,10,15,16], partial coupling of basement and cover rocks may instead enable the Indian basement to drag the cover northwards, generating the sharp syntaxis around the Sibi Trough (inset, Fig. 1a). Similar correspondences between low-angle thrusting and local absence of salt are observed within syntaxes and embayments of other active fold–thrust belts in south Asia[19–21].

The southeastern fringe ellipse is caused by slip on another northeast-dipping reverse fault (labelled F2 in Fig. 1d,e) with a moment magnitude of 6.8. The F2 fault is spatially distinct from F1, being offset southwards, steeper (dip 31°), and shallower (slip is centred at ~9 km, within the sedimentary cover rather than along the basement interface), and there is no indication of any slip connecting the two structures. F2 coseismic uplift is centred along the prominent Tadri anticline (Fig. 1a), which may be a fault

propagation or fault bend fold controlled by underlying reverse slip.

We also find that additional reverse slip totalling M_w 6.1 on a third, subsidiary structure (labelled F3 in Fig. 1d,e) is required to fit a minor east–west phase discontinuity in the southern part of the central fringe pattern. However, its shallow depth extents (0–5 km), elongate dimensions (~20 km) and close spatial correspondence with steep, overturned strata belonging to the southern limb of the Khand Sepal anticline (Fig. 1a) suggest that it represents minor bedding plane slip rather than primary earthquake faulting. This deformation resembles afterslip observed along small faults and folds within the hanging walls of a cluster of large earthquakes near Sefidabeh in Iran[22], and we suspect that slip associated with model fault F3 also occurred post-seismically.

Timing and spacing of seismic slip from arrival times

The InSAR models capture the cumulative surface deformation between May 1996 and May 1999 but what are the relative contributions from seismic slip in the 27 February 1997 earthquake, subsequent aftershocks, and aseismic afterslip? We use seismology to help disentangle the temporal evolution of the signals contained in the interferogram and to provide independent constraints on fault geometry.

With no local network in place, we are restricted to using Global Seismographic Network seismograms at teleseismic distances, augmented by a few regional stations. Teleseismic broadband, vertical component seismograms (Fig. 2a) indicate an abrupt, positive (upwards) arrival that postdates the initial P-wave by 16–17 s at eastern and southeastern azimuths, by 18–0 s at northern
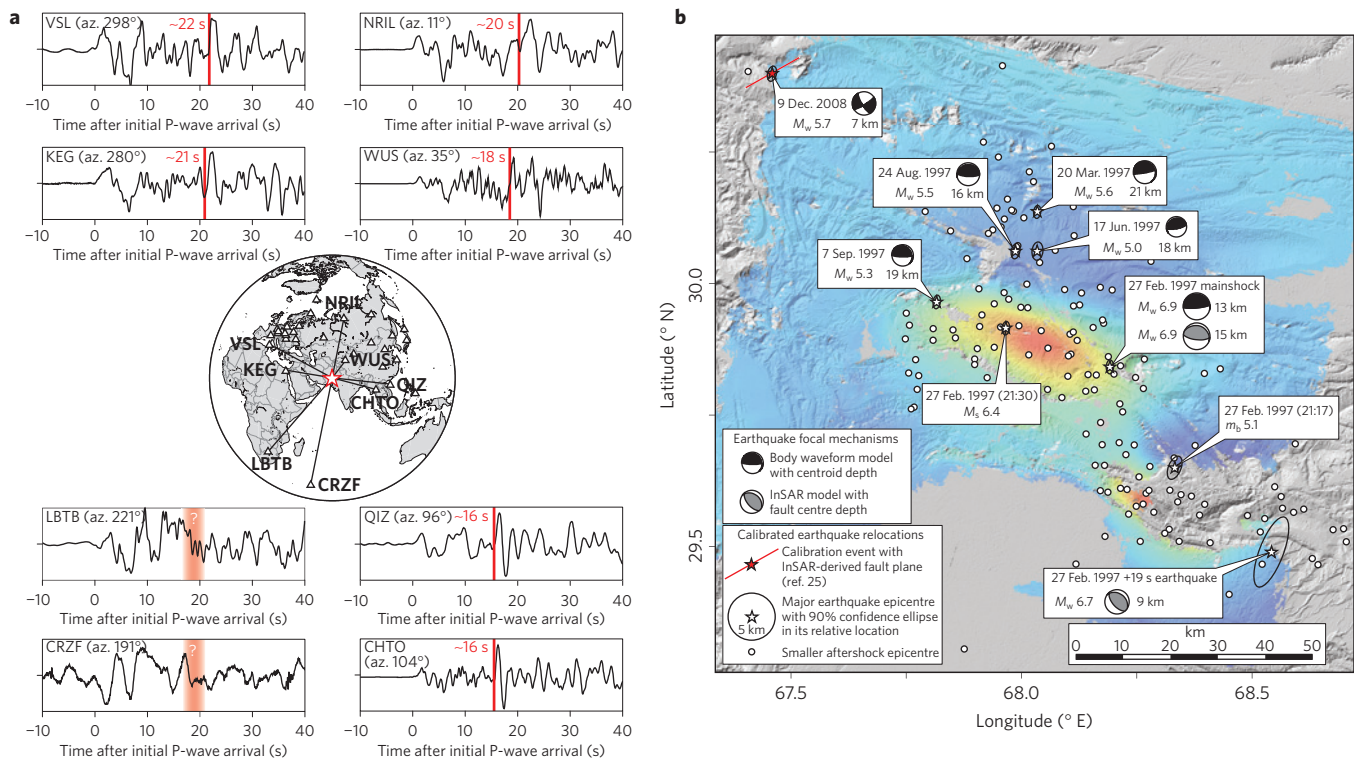
Figure 2 | Seismograms and relocated epicentres. a, Broadband, vertical component seismograms demonstrating the azimuthal variation in delay between Harnai mainshock and +19 s earthquake P-wave arrivals. Lobatse, Botswana (LBTB) and Port Alfred, Crozet Islands (CRZF) are not expected to show impulsive arrivals for the second event. Map shows all stations used in the relocation. VSL, Villasalto, Italy; NRIL, Noril'sk, Russia; KEG, Kottomaia, Egypt; WUS, Wushi, China; QIZ, Qiongzhong, China; CHTO, Chiang Mai, Thailand. **b**, Calibrated epicentres for the mainshock, +19 s earthquake, six major aftershocks (stars), and ~150 smaller aftershocks (circles), plotted over the interferogram from Fig. 1b. Focal mechanisms from body waveform or InSAR modelling are indicated. To calibrate the cluster we used the 2008 Ziarat earthquake[25–27], assuming that its epicentre (red star) lies at the centre of an InSAR-derived model fault[25] (red line).

and northeastern azimuths, and by 21–22 s at western and northwestern azimuths. This azimuthal variation is consistent with a second earthquake that initiates southeast of the first after a delay of ~19 s. Henceforth, we refer to these two, distinct events as the Harnai mainshock and +19 s aftershock. It is difficult to identify the second arrival at southwestern azimuths, where stations lie close to the southwest-dipping auxiliary plane of the InSAR-derived F2 focal sphere (Fig. 2b); at southern azimuths, stations are located on ocean islands and detection is hampered by oceanic noise.

We used a multiple-earthquake relocation technique[23,24] to better define the spatial relationship between the epicentres of the mainshock, the +19 s earthquake, and later aftershocks (Fig. 2b; see Methods). To calibrate the cluster we exploited the 9 December 2008 Ziarat earthquake (M_w 5.7) which occurred in the northwestern part of Fig. 2b and whose surface trace is known from InSAR observations[25–27]. The relocated mainshock epicentre lies at the southeastern end of the F1 model fault (12–14 km south of the published catalogue epicentres), indicating that this fault ruptured first. The epicentral location with respect to the surface deformation implies that mainshock slip then propagated northwestwards along the F1 fault, generating the broad InSAR signal in the centre of the interferograms. The relocated +19 s aftershock epicentre lies ~50 km southeast of the mainshock epicentre near the southeastern end of the F2 fault, at a location in which model slip is restricted to depths of 11–17 km (Fig. 1e). To generate the southeastern fringe ellipse, the +19 s event must then have ruptured unilaterally towards the northwest and from near the bottom upwards.

Later aftershocks are mostly concentrated within or around the edges of the two main fringe ellipses in the interferograms, although of these only the 27 February 21:30 UTC (M_s 6.4) earthquake is

probably large enough to have made a significant contributions to the InSAR deformation. It occurred west of the mainshock hypocentre and may have ruptured or re-ruptured the western part of the F1 slip patch, although we have no independent constraints on its mechanism. Hypocentre locations and source parameters obtained from modelling long-period teleseismic body waveforms[19,28] (see Methods) indicate that the 20 March (M_w 5.6), 17 June (M_w 5.0), 24 August (M_w 5.5) and 7 September 1997 (M_w 5.3) aftershocks probably ruptured the down-dip extension of the Harnai mainshock fault plane (Fig. 2b). Crucially, the largest catalogued aftershock associated with the southeastern fringe ellipse is just body wave magnitude m_b 5.1 and is thus much too small to have generated the surface deformation associated with the F2 fault (M_w 6.8). This discounts a later aftershock as the cause of the F2 faulting.

Slip timing, spacing and scaling from back-projections

Seismic back-projections confirm our proposed model of the spatial and temporal relationship between the Harnai mainshock and +19 s aftershock and provide independent seismological evidence in favour of their comparable magnitudes. Using two dense arrays of teleseismic broadband stations centred in Europe (Fig. 3a) and North America (Fig. 3d), we back-projected coherent P-wave energy onto a grid surrounding the source region over a 2 min period spanning both the mainshock and aftershock[29,30]. Both back-projections show two distinct peaks in stacked energy, separated by ~18 s (Fig. 3b,e and Supplementary Movies 1 and 2). The two peaks have very similar shapes and amplitudes, consistent with comparable moment release in each event. Spatially, the distance and azimuth between the two peaks (31 km and 135° for the EU back-projection, and 41 km and 146° for the North American
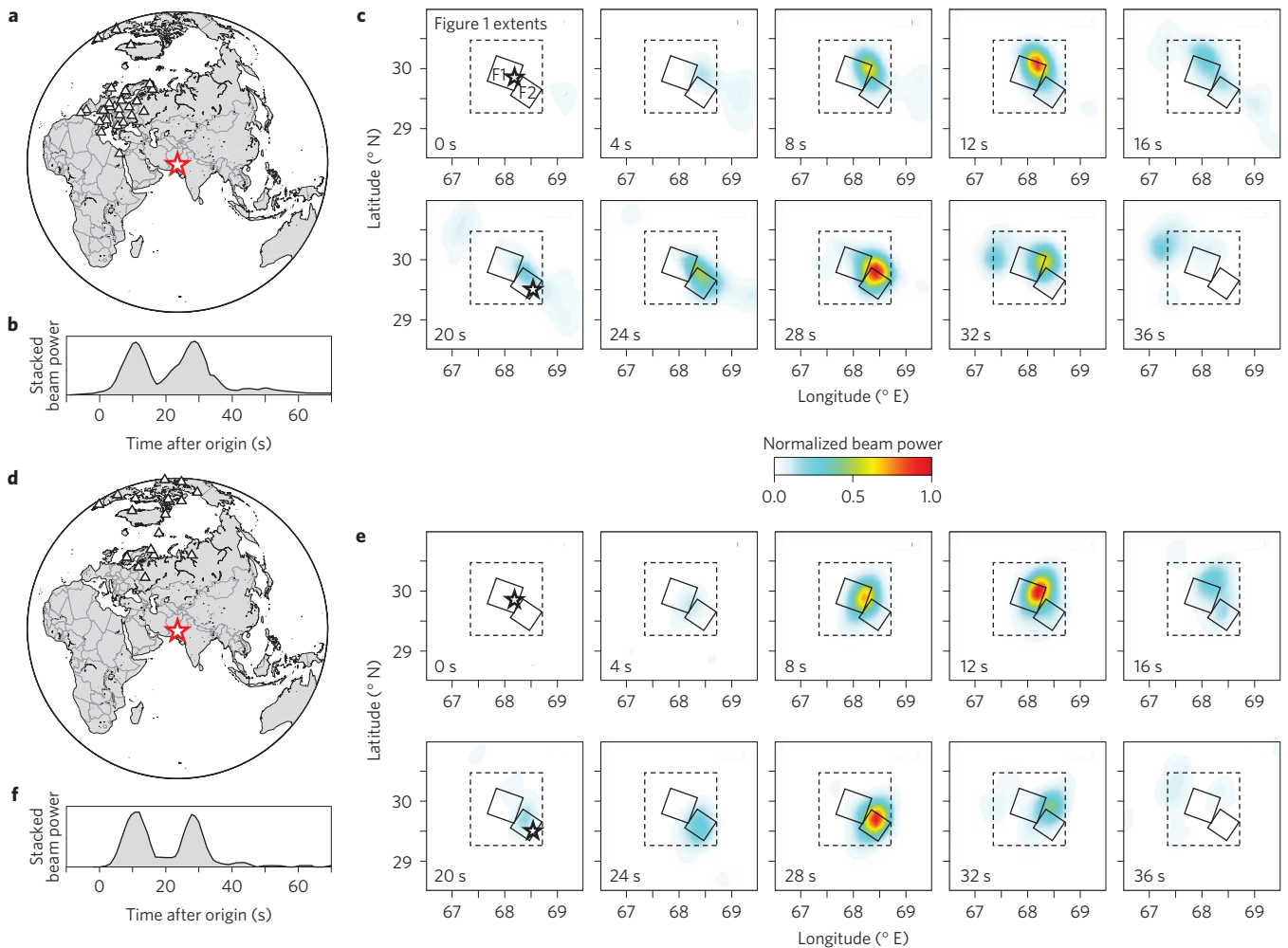
Figure 3 | Seismic back-projections. a, Back-projection array constructed mostly from European seismic stations. **b**, Normalized peak beam power stacked over all grid points. **c**, Snapshots of coherent energy plotted at 4 s intervals after the initial rupture. For reference, the stars in the 0 s and 20 s plots indicate the relocated epicentres of the mainshock and +19 s earthquake, respectively (Fig. 2b), and the small rectangles outline the F1 and F2 model faults (Fig. 1d,e). **d–f**, Back-projection from an array constructed mostly from North American stations, with details as in **a–c**.

back-projection) are consistent with those separating the InSAR-derived F1 and F2 model fault centre coordinates (49 km and 141°). This rules out aseismic afterslip as the source of the southeastern deformation lobe, because this would leave the second, southeastern peak in seismic radiation completely unaccounted for.

Triggering mechanism

We have established that the M_w 7.0 Harnai mainshock was followed ~19 s later by a M_w 6.8 aftershock, initiating ~50 km to the southeast on a spatially distinct fault, but what is the causal relationship between the two earthquakes?

First, we investigate whether permanent (static) stress changes, imparted by mainshock fault slip on the surrounding medium once the seismic vibrations have ceased, promoted failure of an aftershock fault, which was presumably also late in its earthquake cycle and critically stressed[31]. We calculated the static Coulomb failure stress change on the aftershock ('receiver') fault caused by slip on the mainshock ('source') fault[32], using the F2 and F1 fault plane parameters, preferred F1 slip distribution, and the same elastic moduli as in our InSAR modelling. Positive Coulomb stresses mean that receiver faults are brought closer to failure (through an increase in shear stresses and/or a decrease in normal stresses), whereas negative Coulomb stresses mean that receiver faults are brought further from failure. Coulomb stresses beneath the aftershock

epicentre are negative over its inferred nucleation depth range of 11–17 km (Fig. 4a), with a value of −0.003 MPa at the minimum-misfit hypocentre location itself (Fig. 4b).

To test the robustness of this result, we repeated the calculation using perturbed source and receiver fault orientations and source slip distributions. Fault strikes, dips and rakes were varied within their formal error bounds, and alternative source fault slip distributions were generated using a range of slip smoothing factors (see Methods and Supplementary Figs 3–5). Perturbing either the source fault parameters or slip distribution has no discernible impact on Coulomb stress changes at the aftershock hypocentre. Changing the receiver fault orientation has a larger effect (Supplementary Fig. 6), in some instances raising the Coulomb stresses at the aftershock hypocentre to as much as −0.001 MPa, but never to positive values. We also investigated the temporal progression in static stress change on the aftershock fault by determining static Coulomb stresses generated by each 2-second increment in accumulated F1 slip. Assuming a unilateral F1 rupture propagating from southeast to northwest at 2.5 km s⁻¹ (see Methods), we find that Coulomb stress changes at the aftershock hypocentre are negative for the complete duration of F1 rupture (Supplementary Fig. 7).

Although certain limitations to our modelling—namely assumptions of planar faults with uniform rake embedded within
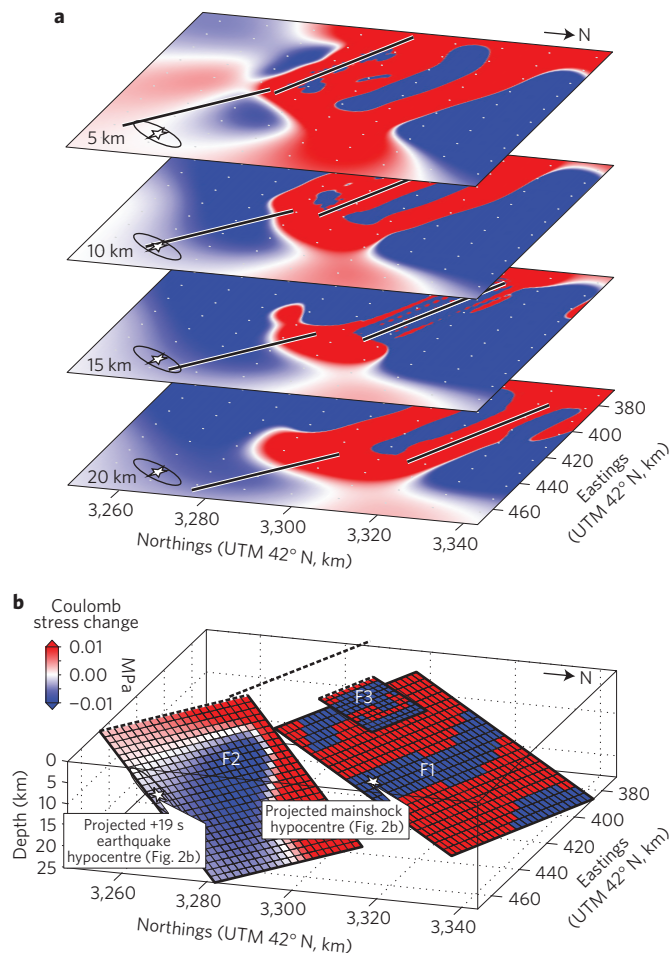
Figure 4 | Coulomb stress changes. a, Coulomb stress changes caused by slip on northeast-dipping source fault F1 at 5 km depth intervals for receiver faults with the same orientation as F2. The +19 s earthquake epicentre is plotted with the 90% confidence ellipse in its relative location (Fig. 2b); its hypocentre depth is probably 11–17 km. **b**, Coulomb stress change resolved onto each receiver fault caused by slip on source fault F1.

small magnitudes and often occur in volcanic or geothermal areas with quite different stress and frictional regimes[34–36]. A notable exception was a M_w 6.9 earthquake in Japan that initiated during the passage of surface waves from a M_w 6.6 event in Indonesia, confirming the potential for larger triggered earthquakes in compressive environments[37]. However, whether dynamic triggering also occurs locally (within 1–2 fault lengths of the triggering event) is still controversial, in part because deconvolving static and transient stress changes within this area is challenging[38–41]. On the one hand, asymmetric aftershock distributions for earthquakes that exhibit a strong rupture directivity[42], and raised aftershock rates for impulsive earthquakes compared with aseismic slip events of the same magnitude[43], both hint at the occurrence of dynamic triggering within the source region. On the other hand, the high-amplitude surface waves that impart the largest transient stresses only fully emerge at much larger distances, leading to the very feasibility of dynamic triggering in the near field (tens of kilometres) being questioned[44].

Our results indicate that large earthquakes can indeed be triggered at such short distances by transient stresses. However, without better constraints on local seismic velocities or any local stations, and given the likelihood of complex wave interactions within the folded and faulted sedimentary cover, we are unable to determine the wave type responsible for triggering the +19 s aftershock. It is therefore unclear whether reductions in the normal stresses on the aftershock fault, increases in shearing stresses, changes to pore fluid pressure, or a combination of these factors was responsible. As static stresses are only fully transmitted once the seismic waves have passed by, we cannot establish what proportion of the (negative) static stress change from F1 slip was felt at the aftershock hypocentre at its origin time, and hence we are unable to place even a lower bound on the (positive) dynamic triggering stress.

Compilations of historical surface rupture traces have been used to imply that fault segment gaps of ~5 km are sufficient to halt an earthquake rupture[1,2]. This figure is also in broad agreement with numerical earthquake simulations[45]. The notion that segment boundaries larger than 5 km will always arrest slip has since been incorporated into the state-of-the-art UCERF3 rupture forecast models for California[3,4]. Yet a few earthquakes are known to have bridged larger segment boundary distances. Surface traces of the 1932 Chang Ma, China ($M \sim 7.6$) and 1896 Rikuu, Japan ($M \sim 7.5$) reverse-faulting earthquakes contain gaps of 10 km and 15 km, respectively[46], and the complex M_w 8.6 Indian Ocean intraplate earthquake of 11 April 2012 bridged a gap of ~20 km between subparallel, but separate, strike-slip faults[47]. However, these events are much larger than the Harnai earthquake and it is possible that in each case static stresses were sufficiently large to trigger slip at distances of 10–20 km.

The Harnai doublet is unprecedented amongst modern, well-recorded events in involving near-instantaneous triggering at a distance of ~50 km, probably through dynamic rather than static stress transfer. The second earthquake increased the eventual seismic moment by ~50% and doubled both the duration of ground shaking and the area affected by the strongest shaking, illustrating the added danger posed by multi-fault ruptures of this type. The implications of this behaviour are especially relevant to other continental fold-and-thrust belts. Earthquake dimensions in these settings are often obscured owing to loss of near-surface slip to folding, limiting the value of historical surface rupture catalogues in anticipating earthquake arrest[45]. As joint geodetic and seismological analyses are not yet standardized, it is unclear how exceptional triggering of the type observed in the Harnai doublet is. A comparison between geologic slip rates and historical earthquake occurrence suggests that multi-segment earthquakes with larger-than-expected magnitudes may be rather frequent amongst the reverse faults of the Los Angeles basin and surroundings[48]. Our results indicate that multiple-fault

a uniform elastic half-space—do not permit us to definitively rule out small, positive Coulomb stresses at the location of aftershock initiation, all available evidence therefore suggests that static stresses imparted by mainshock slip on the F1 fault brought the aftershock fault further from failure, not closer. This implies that the +19 s aftershock was triggered instead by transient (dynamic) stresses generated by the passing seismic waves.

We have no direct constraints on seismic velocities in the sequence of cover rocks above and between the F1 and F2 faults, but we can place conservative bounds of 4–7 km s^{-1} for average P-wave velocities and 2–4 km s^{-1} for shear- and surface-wave velocities. This would indicate that the +19 s aftershock initiated several (~6–12) seconds after passage of P-waves originating at the mainshock hypocentre, at about the same time as the first S-wave and emergent surface wave arrivals, and also at around the same time as passage of P-waves generated along the northwestern F1 fault.

Of these wave types, surface waves are most commonly attributed to suspected cases of dynamic triggering owing to their larger amplitudes, although body waves have also been implicated in sequences of deep focus earthquakes[33]. Great earthquakes commonly generate both instantaneous and delayed seismicity at distances of hundreds to thousands of kilometres, where static stress changes are negligible, but these remote aftershocks usually have

ruptures (as opposed to merely multiple-segment ones), such as sequential failure of the Sierra Madre and Puente Hills thrusts which are separated by ∼20 km, are also mechanically feasible if both systems are critically stressed. Rupture forecast models that prohibit triggering over such length- and time-scales are likely to be overly optimistic in anticipating earthquake hazard in areas that contain dense networks of active faults.

Methods

Methods and any associated references are available in the online version of the paper.

References

1. Wesnousky, S. G. Predicting the endpoints of earthquake ruptures. *Nature* **444**, 358–360 (2006).
2. Wesnousky, S. G. Displacement and geometrical characteristics of earthquake surface ruptures: issues and implications for seismic-hazard analysis and the process of earthquake rupture. *Bull. Seismol. Soc. Am.* **98**, 1609–1632 (2008).
3. Field, E. H. *et al*. Uniform California earthquake rupture forecast, version 3 (UCERF3)—the time-independent model. *Bull. Seismol. Soc. Am.* **104**, 1122–1180 (2014).
4. Page, M. T., Field, E. H., Milner, K. R. & Powers, P. M. The UCERF3 grand inversion: solving for the long-term rate of ruptures in a fault system. *Bull. Seismol. Soc. Am.* **104**, 1181–1204 (2014).
5. Ambraseys, N. & Bilham, R. Earthquakes and associated deformation in northern Baluchistan 1892–2001. *Bull. Seismol. Soc. Am.* **93**, 1573–1605 (2003).
6. Nakata, T., Otsuki, K. & Khan, S. H. Active faults, stress field and plate motion along the Indo-Eurasian plate boundary. *Tectonophysics* **181**, 83–95 (1990).
7. Haq, S. S. & Davis, D. M. Oblique convergence and the lobate mountain belts of western Pakistan. *Geology* **25**, 23–26 (1997).
8. Sarwar, G. & DeJong, K. A. *Geodynamics of Pakistan* 351–358 (Geological Survey of Pakistan, 1979).
9. Banks, C. J. & Warburton, J. 'Passive-roof' duplex geometry in the frontal structures of the Kirthar and Sulaiman mountain belts, Pakistan. *J. Struct. Geol.* **8**, 229–237 (1986).
10. Humayon, M., Lillie, R. J. & Lawrence, R. D. Structural interpretation of the eastern Sulaiman foldbelt and foredeep, Pakistan. *Tectonics* **10**, 299–324 (1991).
11. Davis, D. M. & Lillie, R. J. Changing mechanical response during continental collision: active examples from the foreland thrust belts of Pakistan. *J. Struct. Geol.* **16**, 21–34 (1994).
12. Jadoon, I. A., Lawrence, R. D. & Shahid Hassan, K. Mari-Bugti pop-up zone in the central Sulaiman fold belt, Pakistan. *J. Struct. Geol.* **16**, 147–158 (1994).
13. Bernard, M., Shen-Tu, B., Holt, W. E. & Davis, D. M. Kinematics of active deformation in the Sulaiman Lobe and Range, Pakistan. *J. Geophys. Res.* **105**, 13253–13279 (2000).
14. Copley, A. The formation of mountain range curvature by gravitational spreading. *Earth Planet. Sci. Lett.* **351**, 208–214 (2012).
15. Reynolds, K., Copley, A. & Hussain, E. Evolution and dynamics of a fold-thrust belt: the Sulaiman Range of Pakistan. *Geophys. J. Int.* **201**, 683–710 (2015).
16. Macedo, J. & Marshak, S. Controls on the geometry of fold-thrust belt salients. *Geol. Soc. Am. Bull.* **111**, 1808–1822 (1999).
17. Wright, T. J., Lu, Z. & Wicks, C. Source model for the M_w 6.7, 23 October 2002, Nenana Mountain Earthquake (Alaska) from InSAR. *Geophys. Res. Lett.* **30**, 1974 (2003).
18. Funning, G. J., Parsons, B., Wright, T. J., Jackson, J. A. & Fielding, E. J. Surface displacements and source parameters of the 2003 Bam (Iran) earthquake from Envisat advanced synthetic aperture radar imagery. *J. Geophys. Res.* **110**, B09406 (2005).
19. Talebian, M. & Jackson, J. A reappraisal of earthquake focal mechanisms and active shortening in the Zagros mountains of Iran. *Geophys. J. Int.* **156**, 506–526 (2004).
20. Nissen, E., Tatar, M., Jackson, J. A. & Allen, M. B. New views on earthquake faulting in the Zagros fold-and-thrust belt of Iran. *Geophys. J. Int.* **186**, 928–944 (2011).
21. Satyabala, S. P., Yang, Z. & Bilham, R. Stick-slip advance of the Kohat Plateau in Pakistan. *Nature Geosci.* **5**, 147–150 (2012).
22. Copley, A. & Reynolds, K. Imaging topographic growth by long-lived postseismic afterslip at Sefidabeh, east Iran. *Tectonics* **33**, 330–345 (2014).
23. Ritzwoller, M. H., Shapiro, N. M., Levshin, A. L., Bergman, E. A. & Engdahl, E. R. Ability of a global three-dimensional model to locate regional events. *J. Geophys. Res.* **108**, 2353 (2003).
24. Walker, R. T., Bergman, E. A., Szeliga, W. & Fielding, E. J. Insights into the 1968–1997 Dasht-e-Bayaz and Zirkuh earthquake sequences, eastern Iran, from calibrated relocations, InSAR and high-resolution satellite imagery. *Geophys. J. Int.* **187**, 1577–1603 (2011).
25. Szeliga, W. M. *Historical and Modern Seismotectonics of the Indian Plate with an Emphasis on its Western Boundary with the Eurasian Plate* PhD thesis, Univ. Colorado (2010).
26. Pezzo, G., Boncori, J. P. M., Atzori, S., Antonioli, A. & Salvi, S. Deformation of the western Indian Plate boundary: insights from differential and multi-aperture InSAR data inversion for the 2008 Baluchistan (Western Pakistan) seismic sequence. *Geophys. J. Int.* **198**, 25–39 (2014).
27. Pinel-Puysségur, B., Grandin, R., Bollinger, L. & Baudry, C. Multifaulting in a tectonic syntaxis revealed by InSAR: the case of the Ziarat earthquake sequence (Pakistan). *J. Geophys. Res.* **119**, 5838–5854 (2014).
28. Molnar, P. & Lyon-Caen, H. Fault plane solutions of earthquakes and active tectonics of the Tibetan Plateau and its margins. *Geophys. J. Int.* **99**, 123–154 (1989).
29. Ishii, M., Shearer, P. M., Houston, H. & Vidale, J. E. Extent, duration and speed of the 2004 Sumatra–Andaman earthquake imaged by the Hi-Net array. *Nature* **435**, 933–936 (2005).
30. Trabant, C. *et al*. Data products at the IRIS DMC: stepping-stones for research and other applications. *Seismol. Res. Lett.* **83**, 846–854 (2012).
31. Stein, R. S. The role of stress transfer in earthquake occurrence. *Nature* **402**, 605–609 (1999).
32. Lin, J. & Stein, R. S. Stress triggering in thrust and subduction earthquakes and stress interaction between the southern San Andreas and nearby thrust and strike-slip faults. *J. Geophys. Res.* **109**, B02303 (2004).
33. Tibi, R., Wiens, D. A. & Inoue, H. Remote triggering of deep earthquakes in the 2002 Tonga sequences. *Nature* **424**, 921–925 (2003).
34. Hill, D. P. *et al*. Seismicity remotely triggered by the magnitude 7.3 Landers, California, earthquake. *Science* **260**, 1617–1623 (1993).
35. Velasco, A. A., Hernandez, S., Parsons, T. & Pankow, K. Global ubiquity of dynamic earthquake triggering. *Nature Geosci.* **1**, 375–379 (2008).
36. Pollitz, F. F., Stein, R. S., Sevilgen, V. & Bürgmann, R. The 11 April 2012 east Indian Ocean earthquake triggered large aftershocks worldwide. *Nature* **490**, 250–253 (2012).
37. Lin, C. H. Remote triggering of the M_w 6.9 Hokkaido Earthquake as a result of the M_w 6.6 Indonesian earthquake on September 11, 2008. *Terr. Atmos. Ocean. Sci.* **23**, 283–290 (2012).
38. Voisin, C., Campillo, M., Ionescu, I. R., Cotton, F. & Scotti, O. Dynamic versus static stress triggering and friction parameters: inferences from the November 23, 1980, Irpinia earthquake. *J. Geophys. Res.* **105**, 21647–21659 (2000).
39. Felzer, K. R. & Brodsky, E. E. Decay of aftershock density with distance indicates triggering by dynamic stress. *Nature* **441**, 735–738 (2006).
40. Decriem, J. *et al*. The 2008 May 29 earthquake doublet in SW Iceland. *Geophys. J. Int.* **181**, 1128–1146 (2010).
41. Richards-Dinger, K., Stein, R. S. & Toda, S. Decay of aftershock density with distance does not indicate triggering by dynamic stress. *Nature* **467**, 583–586 (2010).
42. Gomberg, J., Bodin, P. & Reasenberg, P. A. Observing earthquakes triggered in the near field by dynamic deformations. *Bull. Seismol. Soc. Am.* **93**, 118–138 (2003).
43. Pollitz, F. F. & Johnston, M. J. Direct test of static stress versus dynamic stress triggering of aftershocks. *Geophys. Res. Lett.* **33**, L15318 (2006).
44. Parsons, T. & Velasco, A. A. On near-source earthquake triggering. *J. Geophys. Res.* **114**, B10307 (2009).
45. Harris, R. A. & Day, S. M. Dynamic 3D simulations of earthquakes on en echelon faults. *Geophys. Res. Lett.* **26**, 2089–2092 (1999).
46. Rubin, C. M. Systematic underestimate of earthquake magnitudes from large intracontinental reverse faults: historical ruptures break across segment boundaries. *Geology* **24**, 989–992 (1996).
47. Meng, L. *et al*. Earthquake in a maze: compressional rupture branching during the 2012 M_w 8.6 Sumatra earthquake. *Science* **337**, 724–726 (2012).
48. Dolan, J. F. *et al*. Prospects for larger or more frequent earthquakes in the Los Angeles Metropolitan region. *Science* **267**, 199–205 (1995).
49. Engdahl, E. R., van der Hilst, R. & Buland, R. Global teleseismic earthquake relocation with improved travel times and procedures for depth determination. *Bull. Seismol. Soc. Am.* **88**, 722–743 (1998).
50. Argus, D. F. *et al*. The angular velocities of the plates and the velocity of Earth's centre from space geodesy. *Geophys. J. Int.* **180**, 913–960 (2010).

Author contributions

InSAR analysis and accompanying Coulomb modelling were undertaken by E.N. and J.R.E. Seismological analyses were led by R.A.S. (calibrated multi-event relocation), A.H. (seismic back-projection) and E.N. (body waveform modelling). All authors contributed to the interpretation of results and E.N. wrote the manuscript.

Additional information

Supplementary information is available in the online version of the paper. Reprints and permissions information is available online at www.nature.com/reprints. Correspondence and requests for materials should be addressed to E.N.

Competing financial interests

The authors declare no competing financial interests.

Methods

InSAR modelling. We used standard elastic dislocation modelling procedures[17,18] to characterize the faulting observed in the interferogram. Line-of-sight displacements were first resampled using a quadtree algorithm, reducing the size of the data set whilst concentrating sampling in areas with high deformation gradients. Representing faults initially as rectangular dislocations buried in an elastic half-space with Lamé parameters $\mu = \lambda = 3.23 \times 10^{10}$ Pa and a Poisson's ratio of 0.25, we used Powell's algorithm with multiple Monte Carlo restarts to obtain the minimum-misfit strike, dip, rake, slip, latitude, longitude, length, and top and bottom depths of each fault, solving simultaneously for a static shift and displacement gradients in the north–south and east–west directions to account for ambiguities in the zero-displacement level and residual orbital phase ramp. Uncertainties in these parameters were then estimated by modelling data sets perturbed by realistic atmospheric noise[17,18].

The broad fringe ellipse in the scene centre can be reproduced by either of two, 39-km-long, M_w 6.9 model faults (labelled F1), the first which dips 22° NE and projects upwards towards the northern Sibi Trough, and the second which dips 63° SW and projects to the surface at the northern edge of the fringe ellipse. Both involve buried reverse slip centred at 15–16 km depth, although slip magnitude is poorly constrained owing to a strong trade-off with fault width. The southeastern deformation pattern can also be reproduced by either of two conjugate, M_w 6.7–6.8 reverse faults (labelled F2), one that dips 31° NE and projects up-dip towards the Sibi Trough, the other that dips 57° SW and projects to the surface north of the Tadri anticline. Model interferograms and residual (model minus observed) displacements for all four uniform slip F1 and F2 fault combinations are shown in Supplementary Fig. 2, with model parameters given in Supplementary Table 2. However, later we will show that only the northeast-dipping F1 and F2 model faults are consistent with teleseismic body waveform analysis and epicentral relocations. Parameter trade-offs and errors for these northeast-dipping model faults are shown in Supplementary Figs 3 and 4.

To explore the slip patterns in more detail, we extended each model fault by a few kilometres beyond its uniform slip bounds, and solved for the distribution of slip over these surfaces using a Laplacian smoothing criterion to ensure realistic slip gradients[17,18]. Fault rakes were fixed to their uniform slip values, reflecting the single available look direction, and a non-negative least-squares algorithm was used to prevent retrograde displacements. The trade-off between slip magnitude and down-dip fault width means that there is no unique solution; instead, a suite of models is generated using a range of smoothing parameters. The preferred model was generated using a scalar smoothing factor of 400 to weight the smoothing[18] (Fig. 1d,e; residual displacements shown in Supplementary Fig. 5c). The F1 slip patch is ~50 km in length, ~15 km in width (its rather elongate dimensions a robust feature of the inversion), centred at ~15 km depth, and has a M_w of 7.0. The F2 slip patch is ~35 km in length, centred at ~9 km depth, with a M_w of 6.8. Its width is less well resolved owing in part to interferometric decorrelation in its hanging wall. Residuals in the areas between the two faults are negligible, implying an absence of slip in the area between the main F1 and F2 slip patches. We also find that additional reverse slip on a third, subsidiary structure is required to fit a minor, east–west phase discontinuity in the southern part of the central fringe pattern. This M_w 6.1 model fault (labelled F3 in Fig. 1d,e) is ~20 km long, dips 18° N and extends from close to the surface to a depth of ~5 km.

Calibrated earthquake relocations. We used a calibrated earthquake relocation technique[23,24] to relocate the epicentres of the Harnai mainshock and 150 of its aftershocks. Multiple-event relocations exploit the fact that although unknown velocity structure along teleseismic ray paths leads to large uncertainties in absolute hypocentre positioning, phases from clusters of nearby earthquakes sample roughly the same portion of the Earth, permitting much tighter constraints on relative hypocentre locations. If the hypocentre of any one (or more) event in the cluster is known independently, the locations for the entire cluster can be calibrated by applying a shift to satisfy these additional constraints. Earthquakes with moderate source dimensions mapped with InSAR are well suited for calibration purposes[24]. In this instance, we exploit an M_w 5.7 strike-slip earthquake that occurred on 9 December 2008 near Ziarat (northwest corner of Fig. 1) and which exhibits a clear, well-defined InSAR signal consistent with a vertical or sub-vertical fault with a strike of 242°–245° and a length of 8–13 km (refs 25–27). We take the centre of a uniform slip model fault[25] as its epicentre, resulting in a ~6.5 km uncertainty in the along-strike direction. This earthquake is spatially separated from the main cluster by several tens of kilometres, and lateral variations in the velocity structure within this region may be an additional source of error. To relocate events in the cluster we used the phase arrival times reported in the ISC bulletin. However, the +19 s aftershock was not reported by the ISC and we instead manually picked P-wave arrivals from 30 stations at regional and teleseismic distances. We purposely avoided using seismograms at distances <20°, because many of these contain complex, refracted head waves which make picking the aftershock arrival difficult. It was also difficult to identify this phase in traces from stations to the southwest, probably because the P-wave arrival is near-nodal at teleseismic distances in this direction, and also from Indian Ocean stations, which are noisy.

Consequently, the confidence ellipse for this event is elongated in the south-southwest–north-northeast direction. During the relocation we excluded the smallest aftershocks for which there were few reported phase arrivals and an insufficient azimuthal coverage to obtain stable epicentres, and we made an empirical estimate of the average reading error for each station–phase pair and 'cleaned' the ISC phase arrival times of clear outliers. The lack of local phase arrival data prevents us from attempting to constrain the hypocentral depths. Our reported locations (Supplementary Table 3) have been determined assuming 15 km hypocentral depths, close to the base of the seismogenic layer in this region[13,15], but using 10 km or 20 km does not significantly change the resulting pattern. Projected onto the northeast-dipping F2 model fault plane, the +19 s aftershock hypocentre coincides on a prominent slip patch at 11–17 km depth (Supplementary Fig. 5a–c). Projected onto the conjugate southwest-dipping F2 model fault, the epicentre lies outside the main slip distribution (Supplementary Fig. 5d–f), and consequently we are able to discount this candidate fault plane.

Teleseismic body waveform modelling. Modelling long-period teleseismic body waveforms provides independent source parameters for the Harnai mainshock and many of its largest aftershocks. In this approach, earthquakes appear as a point source in space (the 'centroid') and are thus insensitive to short-wavelength variation in fault slip and local velocity structure[28]. By accounting for the separation between direct P and S arrivals and near-source surface reflections pP, sP and sS, these methods are known to yield more accurate centroid depths than the solutions reported by the GCMT, NEIC or EHB earthquake catalogues, as well as independent estimates of other focal parameters. In some instances teleseismic body waveform modelling can also reveal distinct sub-events and constrain their timing, depths and mechanisms. We used long-period (15–100 s) seismograms recorded over the distance range 30°–90° (Supplementary Fig. 8). Vertical components were used to model P, pP and sP phases and transverse component seismograms were used for the S and sS phases. Without direct measurements of seismic wave velocities in our region of interest, we assumed a half-space with values of 6.0 km s⁻¹ for the P-wave velocity, 3.5 km s⁻¹ for the S-wave velocity and 2.8×10^3 kg m⁻³ for density, consistent with the elastic half-space structure used in the InSAR modelling. Faster seismic velocities above the earthquake source would result in a shallower centroid depth (and vice versa), whereas the choice of density primarily affects the seismic moment. We used a routine modelling procedure[19,20] that minimizes the misfit between observed and synthetic seismograms to solve for the best-fit strike, dip, rake, scalar moment, centroid depth and source time function of each event. Uncertainties in key parameters of interest were estimated by holding them fixed, inverting for remaining free parameters, and inspecting the degradation in fit between observed and synthetic waveforms[28].

For the initial earthquake, we obtained a good fit to the first ~20 s of the observed waveforms, providing important additional constraints on mainshock mechanism and depth (Fig. 2b and Supplementary Table 1 and Supplementary Fig. 9), but we could not find a stable two-source solution that would also characterize the +19 s aftershock. The gently northeast-dipping mainshock nodal plane strike is relatively poorly constrained at 315° (errors of +20° and −40°), trading off against rake (140°, errors of 20° and −40°) to keep a relatively stable slip vector (176° ± 2°). Within error, this strike thus agrees within that of the northeast-dipping candidate F1 fault (290°), and our preferred body wave solution incorporates the more tightly constrained InSAR-derived strike as a fixed parameter. The strike of the steeper, ~S-dipping body waveform model nodal plane is 86° (errors of +5° and −6°), in clear disagreement with that of the equivalent candidate F1 fault (107°). On this basis, we rule out the southwest-dipping fault plane. The northeast-dipping nodal plane dips at 14° (errors of +8° and −6°), just within error of the InSAR-derived F1 dip of 22°. The centroid depth of 13 km (errors of +1 km and −4 km) trades off against the moment of 2.5 (errors of +0.9 and −0.3) $\times 10^{19}$ Nm, both agreeing to within error with the uniform slip F1 values from initial InSAR modelling. The 20 s duration of the source time function is an especially robust feature of the inversion, closely matching that of the first pulse in the back-projection stacked beam power (Fig. 3b,f). When combined with the ~50 km F1 fault length and the unilateral (southeast to northwest) rupture propagation direction, this result yields an estimated rupture velocity of ~2.5 km s⁻¹. We attempted to characterize the seismograms with a two-source event, fixing the parameters described above for an initial mainshock and then solving for the source parameters (including the azimuth, distance and time delay) of a sub-event. Although the fit between observed and model seismograms can be improved substantially compared with the single-event model, we find that the sub-event mechanism, depth, and time delay are all highly unstable in this inversion. We are therefore unable to provide seismological constraints on the +19 s aftershock focal mechanism that are independent of the InSAR modelling, as we did for the mainshock.

Source parameters obtained for the largest subsequent aftershocks of the Harnai sequence (Fig. 2b and Supplementary Table 4 and Supplementary Figs 10–14) are similar to those obtained previously using body waveform modelling[15], with discrepancies of at most a few degrees in strike, dip and rake, and

up to 2 km in centroid depth. The largest of these (4 March 1997, M_w 5.6) was a strike-slip event that occurred southeast of the map extents of Fig. 2b. The 20 March (M_w 5.6), 17 June (M_w 5.0), 24 August (M_w 5.5) and 7 September 1997 (M_w 5.3) aftershocks have shallow (12°–27°) north- or north-northeast-dipping nodal planes with slip vectors (170°–183°) that cluster around that of the Harnai mainshock (176°). Unfortunately, seismograms of the 27 February 1997 21:17 UTC (m_b 5.1), 21:30 UTC (M_s 6.4) and 22:41 (m_b 5.2) aftershocks were very noisy, preventing us from obtaining robust solutions for these events.

Data and code availability. ERS-2 SAR data are copyrighted by the European Space Agency and the raw single look complex imagery may be obtained from them on request. InSAR processing was performed using ROI_PAC 3.0 software which is freely available from JPL/Caltech (http://www.openchannelfoundation.org/projects/ROI_PAC). Derived interferograms, corresponding metadata and codes for InSAR modelling are available from the authors on request. Coulomb stress modelling was performed using Coulomb 3 software which is freely available from the USGS (http://earthquake.usgs.gov/research/software/coulomb). Seismic arrival time data were obtained from the Bulletin of the International Seismological Centre (http://www.isc.ac.uk/iscbulletin) and modelled using mloc software written by E. Bergman (http://www.seismo.com). Waveform data were accessed through the Incorporated Research Institutions for Seismology (IRIS) Data Management Center (http://ds.iris.edu/ds/nodes/dmc) and modelled using MT5 and back-projection codes that are available from the authors on request.